Applied Mathematics and Computation 248 (2014) 28–46

Contents lists available at ScienceDirect

Applied Mathematics and Computation

journal homepage: www.elsevier.com/locate/amc

Analysis of stability, verification and chaos with the Kreiss–Ystrom equations

William D. Fullmer [a], Martin A. Lopez de Bertodano [a], Min Chen [b], Alejandro Clausse [c,*]

[a] School of Nuclear Engineering, Purdue University, West Lafayette, IN 47907, USA
[b] Department of Mathematics, Purdue University, West Lafayette, IN 47907, USA
[c] CNEA-CONICET and Universidad Nacional del Centro, 7000 Tandil, Argentina

ARTICLE INFO

Keywords:
Ill-posed
Verification
Chaos
Two-fluid model

ABSTRACT

A system of two coupled PDEs originally proposed and studied by Kreiss and Ystrom (2002), which is dynamically similar to a one-dimensional two-fluid model of two-phase flow, is investigated here. It is demonstrated that in the limit of vanishing viscosity (i.e., neglecting second-order and higher derivatives), the system possesses complex eigenvalues and is therefore ill-posed. The regularized problem (i.e., including viscous second-order derivatives) retains the long-wavelength linear instability but with a cut-off wavelength, below which the system is linearly stable and dissipative. A second-order accurate numerical scheme, which is verified using the method of manufactured solutions, is used to simulate the system. For short to intermediate periods of time, numerical solutions compare favorably to those published previously by the original authors. However, the solutions at a later time are considerably different and have the properties of chaos. To quantify the chaos, the largest Lyapunov exponent is calculated and found to be approximately 0.38. Additionally, the correlation dimension of the attractor is assessed, resulting in a fractal dimension of 2.8 with an embedded dimension of approximately 6. Subsequently, the route to chaos is qualitatively explored with investigations of asymptotic stability, traveling-wave limit cycles and intermittency. Finally, the numerical solution, which is grid-dependent in space–time for long times, is demonstrated to be convergent using the time-averaged amplitude spectra.

1. Introduction

The present work focuses on the Kreiss and Ystrom [1] system of partial differential equations (PDEs) given by

$$\frac{\partial \alpha}{\partial t} + u\frac{\partial \alpha}{\partial x} + \left(1 + \frac{\alpha}{2}\right)\frac{\partial u}{\partial x} = \varepsilon \frac{\partial^2 \alpha}{\partial x^2} - 2\alpha, \tag{1}$$

$$\frac{\partial u}{\partial t} + u\frac{\partial u}{\partial x} = C\frac{\partial \alpha}{\partial x} + \nu \frac{\partial^2 u}{\partial x^2}. \tag{2}$$

* Corresponding author.
E-mail addresses: wfullmer@purdue.edu (W.D. Fullmer), bertodan@purdue.edu (M.A. Lopez de Bertodano), chen@math.purdue.edu (M. Chen), clausse@exa.unicen.edu.ar (A. Clausse).

http://dx.doi.org/10.1016/j.amc.2014.09.074
0096-3003/

and hereafter referred to as the KY equations. There are a few slight differences between Eqs. (1) and (2) and the originally published equations, which should be noted. First, the parameter C was simply unity in the original equations. The adjustable coefficient C is used here as a means to vary the "degree of instability." Second, the viscosities have been given different symbols, although the same value will be used for both in the present work. To highlight the similarities between the KY equations and the one-dimensional (1-D) two-fluid model, the symbols of the original variables are renamed α and u.

The KY system is purely mathematical; it was not derived to model a physical problem. However, this work has evolved out of a separate, but related, study of the 1-D two-fluid model, which is a physically based engineering model for two-phase pipe and channel flow. For incompressible and isothermal flow, the full 1-D two-fluid model of Ishii and Hibiki [2] can be reduced to a two-equation model as shown by Lopez de Bertodano, Fullmer and Vaidheeswaran [3]. For the horizontal stratified flow of two fluids with a small density ratio (e.g., ambient air–water), the simplified two equation form is given by

$$\frac{\partial \alpha}{\partial t} + u\frac{\partial \alpha}{\partial x} + \alpha\frac{\partial u}{\partial x} = \varepsilon\frac{\partial^2 \alpha}{\partial x^2} \tag{3}$$

$$\frac{\partial u}{\partial t} + u\frac{\partial u}{\partial x} = C\frac{\partial \alpha}{\partial x} + \nu\frac{\partial^2 u}{\partial x^2} + \tilde{\sigma}\frac{\partial^3 \alpha}{\partial x^3} + F(\alpha, u) \tag{4}$$

where α and u are the liquid void fraction and liquid velocity, respectively. The constants ε, ν and $\tilde{\sigma}$ are the artificial viscosity (if modeled); the kinematic, turbulent or (if modeled) artificial viscosity and the scaled surface tension coefficient, respectively. The function F contains the algebraic closure relations for the wall and interfacial shear models. The coefficient C is related to the Kelvin–Helmholtz instability and is given by $C = r(1-\alpha)^{-1}u_R^2 - g_y H$ where r, u_R, g_y and H are the density ratio, velocity difference between the fluids, normal component of gravity and the channel height, respectively. See Lopez de Bertodano et al. [3] for details of the model and its derivation.

The 1-D two-fluid model and the present KY system are related in several significant ways. Both models are conditionally ill-posed as an initial and boundary value problem (IBVP) without higher order regularization, i.e., the first-order systems (may) possess complex characteristics. Both models are predicted to be unstable in a linear stability sense. The magnitude of the growth rates are linearly proportional to the wavenumber without regularization and quadratically damped at high-wavenumbers with higher-order regularization. Both models have similar dynamics, i.e., they produce similar waveforms (compare Fig. 5 of the present work with Fig. 11 of Fullmer, Ransom and Lopez de Bertodano [4]). However, the mathematical system of Kreiss and Ystrom [1] is simpler in several desirable ways. It does not have a complicated flow-regime map of closure laws for different flow conditions – some of which affect the differential form of the governing equations. The dynamics of the problem are not bounded by physical limitations, e.g., channel height. It does not require special numerical techniques. Finally, and possible most importantly, the "degree of instability" can be directly controlled by specifying the constant value of C in Eqs. (1) and (2). In the 1-D two-fluid model of Eqs. (3) and (4), the coefficient equivalent to C is not a constant, but instead, it is determined by the local flow conditions so that the linear stability of the model changes throughout the solution – and may even change from non-hyperbolic to hyperbolic depending on the flow conditions. Therefore, the simplified form and added control of the KY equations make it ideal for the type of studies undertaken here.

The linear stability of the system will be reviewed in Section 2. The numerical method used to solve the equations is outlined in Section 3 followed by a verification study of the code in Section 4. Some nonlinear solutions are given in Section 5 along with a hint that the system may by chaotic, which is proven in Section 6 together with a brief exploration of the route to chaos. Finally, in Section 7, the subject of solution verification is revisited and reinterpreted with the knowledge that the system is chaotic.

2. Linear stability analysis

2.1. Characteristic analysis

The KY Eqs. (1) and (2) can be written in vector form as

$$\frac{\partial \phi}{\partial t} + \mathbf{A}\frac{\partial \phi}{\partial x} - \mathbf{D}\frac{\partial^2 \phi}{\partial x^2} + F = 0, \tag{5}$$

where the dependent variable vector is $\phi = (\,\alpha \quad u\,)^T$, the source vector is $F = (\,2\alpha \quad 0\,)^T$ and the coefficient matrices are defined by

$$\mathbf{A} = \begin{pmatrix} u & 1+\alpha/2 \\ -C & u \end{pmatrix} \quad \mathbf{D} = \begin{pmatrix} \varepsilon & 0 \\ 0 & \nu \end{pmatrix}. \tag{6}$$

The eigenvalues of $\mathbf{A}$ are given by

$$\xi = u \pm i\sqrt{C(1+\alpha/2)} \tag{7}$$

In the absence of diffusion, i.e., $\varepsilon = \nu = 0$, these eigenvalues define the characteristics of the system. Eq. (7) shows that for $C > 0$ (and $\alpha > -2$) the characteristics are complex conjugates. Therefore, the system is elliptic and ill-posed as an IBVP. Even when the diffusion matrix is included, the complex characteristics are the root cause of the linear growth discussed below. In

contrast, for $C < 0$ (and $\alpha > -2$), the characteristics are both real, and the system is hyperbolic. In this case, the problem simplifies dramatically, and the KY equations are similar to a modified shallow-water model. There is a large body of work concerning the nature of shallow-water equations; therefore, the hyperbolic case is not of primary interest in this paper. Equivalent but opposite classifications occur for the case $\alpha < -2$, which is also not studied here.

2.2. Fourier analysis

To better highlight the effect of the diffusion terms, the equations are linearized about an initial reference state with an infinitesimally small perturbation superimposed: $\phi = \phi_0 + \phi'$. The solution is inserted into Eq. (5), and three assumptions are applied to greatly simplify the resulting equation: the initial reference state satisfies Eq. (5) automatically, the products of the perturbations are negligible and the reference state is either steady or the length scale of the reference state is considerably larger than that of the imposed perturbation, i.e., $\partial\phi_0/\partial x \ll \partial\phi'/\partial x$. The remaining terms define the linear perturbation equation

$$\frac{\partial \phi'}{\partial t} + \mathbf{A}_0 \frac{\partial \phi'}{\partial x} - \mathbf{D}\frac{\partial^2 \phi'}{\partial x^2} + \frac{\partial F_0}{\partial \phi'^T}\phi' = 0, \tag{8}$$

where $\mathbf{A}_0$ and F_0 are evaluated at ϕ_0. In typical fashion, the perturbation is assumed to be a traveling wave

$$\phi' = \hat{\phi}' e^{i(\kappa x - \omega t)}, \tag{9}$$

where $\hat{\phi}'$ is the amplitude, κ is the wavenumber and ω is the angular frequency. The more intuitive variables of wavelength and frequency are related by $\lambda = 2\pi/\kappa$ and $f = \omega/2\pi$, respectively. In general, the angular frequency may be complex, and from Eq. (9), when the imaginary component is positive, the perturbation will grow exponentially in time. The real component of the angular frequency and the wavenumber define the wave speed, $c = \omega_R/\kappa$.

Inserting Eq. (9) into Eq. (8) gives

$$\left(-i\omega + i\kappa\mathbf{A}_0 - (i\kappa)^2\mathbf{D} + \frac{\partial F_0}{\partial \phi'^T}\right)\phi' = 0. \tag{10}$$

For a nontrivial solution to exist, the coefficient matrix of Eq. (10) must be singular, i.e.,

$$\det\left[\left(\omega - \kappa\mathbf{A}_0 + i\kappa^2\mathbf{D} + i\frac{\partial F_0}{\partial \phi'^T}\right)\right] = 0 \tag{11}$$

Solving Eq. (11) for the angular frequency gives

$$\omega = \kappa u_0 - \frac{i}{2}\left[(\varepsilon + \nu)\kappa^2 + 2 \pm \sqrt{((\varepsilon - \nu)\kappa^2 + 2)^2 + (2\xi_I\kappa)^2}\right], \tag{12}$$

where ξ_I is the imaginary component of the eigenvalues previously derived in Eq. (7). The larger imaginary root of the angular frequency is shown in Fig. 1 for a reference state of $\alpha_0 = u_0 = 1$ and $C = 1$.

It is readily observed from Eq. (12) that, if diffusion is neglected, $\varepsilon = \nu = 0$, the growth rate, ω_I, will have a positive and negative component indicating exponential growth. In the limit $\kappa \to \infty$, the characteristics in Eq. (7) are recovered using ω/κ in Eq. (12). The ill-posedness of the system is obvious: an infinitely short wavelength perturbation ($\kappa \to \infty$) has an infinitely large growth rate ($\omega_I \to \infty$). For large κ, the growth rate is approximately linear with respect to κ with a small, constant damping due to the source term. The linear growth rate is also observed in the 1-D two-fluid model under certain conditions and is a characteristic feature of the Kelvin–Helmholtz instability that is imbedded within the model equations.

If one of the diffusion coefficients (viscosities) is set to a positive constant value, the linear dependence is suppressed at large wavenumbers, and the growth rate approaches an asymptotic value. From a practical point of view, this appears to be of little value because the largest growth rate still occurs at the smallest scales. In fact, even the ill-posed differential model avoids the singularity because, in most applications, the equations are solved in some discrete fashion limiting the maximum growth rate to some finite value related to the resolution of the discretization.

Now, if both viscosities are positive constants, the linear stability changes even more dramatically; rather than approaching an asymptote, the stability curve bends down and approaches negative infinity as $\kappa \to \infty$. For the special case $\varepsilon = \nu$, the imaginary part of Eq. (12) reduces to three components: a negative constant component from the source term, a positive linear component from the underlying ill-posedness and a quadratic negative term from the diffusion terms. The combined result is that the growth rate is positive for a wavenumber in the range from $\kappa \in (0, \kappa_0)$ and negative for $\kappa \in (\kappa_0, \infty)$, as shown in Fig. 1. The value of the cut off wavenumber is given by $\kappa_0 = \nu^{-1}\sqrt{\xi_I^2 - 2\nu}$. In the growth region, there is a single maximum growth rate, the critical growth rate, given by $\omega_c = \xi_I^2/4\nu + \nu/\xi_I^2 - 1$, which occurs at the critical wavenumber $\kappa_c = \sqrt{\xi_I^2/4\nu^2 - 1/\xi_I^2}$. While there is still exponential growth, this type of linear instability is physically acceptable. The perturbations will grow if the wavelength is long enough and decay at short length scales. Lastly, it should be noted that the KY

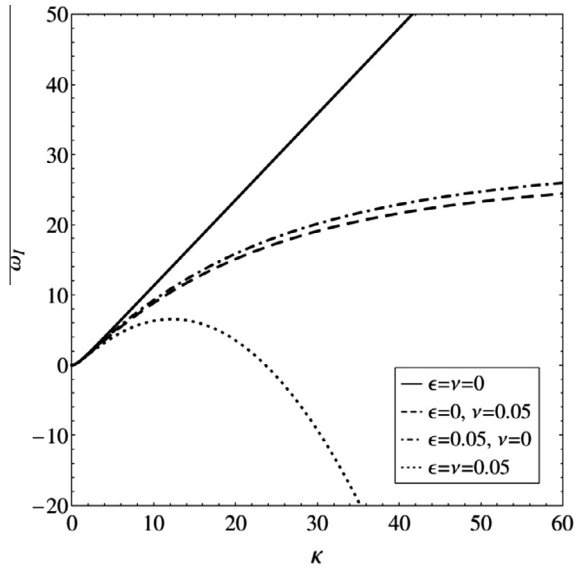

Fig. 1. Effect of the higher-order regularization (diffusion) on the linear growth rate.

equations are not dispersive in any case because the real part of the angular frequency is always linear in κ so that the wave speed is constant, $c = u$ [5].

The linear stability properties of the KY equations and how it is affected by the viscosities parallel that of the 1-D two-fluid model [4,6]. In particular, to achieve a cut-off wavenumber beyond which perturbations decay, second-order diffusion terms must be added to all equations even when there is no physical justification. It is worth noting that both the 1-D two-fluid model and the KY equations can also be regularized using a combination of kinematic or turbulent viscosity and a third-order term related to surface tension. This approach introduces dispersion, which increases the complexity of the problem and will not be explored here. Finally, it is noted that, while a very simple approach to linear stability has been taken here, it is sufficient to guide the nonlinear simulations that follow. See the original work of Kreiss and Ystrom [1] for a more comprehensive analysis.

3. Numerical method

3.1. Structure

The numerical method used to solve the KY equations will be outlined and briefly discussed. The structure of the finite difference method is similar to that used for a higher-order 1-D two-fluid model pilot code by Fullmer, Lopez de Bertodano and Zhang [7]. However, the simpler KY equations are free from some of the numerical constraints that otherwise limit the flexibility of 1-D two-fluid model algorithms, e.g., pressure–velocity coupling, volume fraction-energy coupling, water packing mitigation, etc.

The basic underlying structure utilizes a staggered grid common in computational fluid flow problems. A domain of length L is discretized into N cells of uniform length $\Delta x = L/N$ with $N + 1$ faces at edge of each cell. The α variable is stored at the cell centers, and the u variable is stored at cell faces. A sketch of the grid in the vicinity of a cell center, i, and face, j, is shown in Fig. 2.

Eq. (5) is arranged into the form

$$\frac{\partial \phi}{\partial t} = f_\phi(\alpha^{n\pm k}, u^{n\pm k}, t^{n\pm k}), \tag{13}$$

where the right hand side functions, f_ϕ, are assumed to be known at each time level $n \pm k$ through a finite-difference scheme, and the time is advanced by treating the PDE as $2N$ ordinary differential equations (ODEs). The finite-difference functions are given by

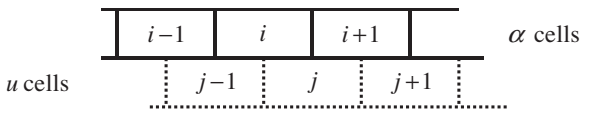

Fig. 2. A sketch of the staggered grid used for the finite difference equations.

$$f_{\alpha,i} = -\bar{u}\frac{\hat{\alpha}_R - \hat{\alpha}_L}{\Delta x} - \left(1 + \frac{\alpha_i}{2}\right)\frac{u_R - u_L}{\Delta x} + \varepsilon\frac{\alpha_{i+1} - 2\alpha_i + \alpha_{i-1}}{\Delta x^2} - 2\alpha_i + S_{\alpha,i} \tag{14}$$

for the α equation at location i and

$$f_{u,j} = -u_j\frac{\hat{u}_R - \hat{u}_L}{\Delta x} + C\frac{\alpha_R - \alpha_L}{\Delta x} + \nu\frac{u_{j+1} - 2u_j + u_{j-1}}{\Delta x^2} + S_{u,j} \tag{15}$$

for the u equation at location j. The overbar indicates a cell averaged (mean) value. Variables with a hat do not exist at the specified location. The additional subscripts refer to the values to the "right" and "left" of the reference location. For example, in Eq. (14) the faces j and $j+1$ surround reference position i (likewise for Eq. (15) the cell centers $i-1$ and i surround reference position j). When the variables required at the right and left are available, they are used directly, e.g., u exists at j and $j+1$ in Eq. (14). When the variables do not exist in the locations to the right and left, as indicated by the hat, they are donored or extrapolated using the values at the neighboring locations. A flux-limiter is used for the extrapolation and discussed in the following section. The diffusion terms are discretized using a standard second-order center difference scheme. An additional source term appears in each equation, $S_{\alpha,i}$ and $S_{u,j}$, which is not part of the original KY equations but has been added here for future use. For all simulations in the present work, periodic boundary conditions are applied, which is achieved by placing three "ghost" cells at the beginning and end of the domain that mirror the conditions at the opposite end.

3.2. Flux limiter

For the extrapolated variables, there are many options. Two obvious choices are first-order upwinding (FOU) and center differencing. Viewing the KY equations as an odd distillation of the 1-D two-fluid model, one would choose upwinding with edge values simply donored from the adjacent values in the direction of the flow. The FOU method is still utilized in most industrial 1-D two-fluid model codes due to its stability and robustness. The problem is that applying the FOU method to the convection variables adds a significant amount of numerical diffusion and lowers the accuracy of the entire scheme. In contrast, viewing the KY equations as simply two mathematical PDEs, independent of physics, one might opt for a center difference scheme. However, this approach would leave the overall finite difference scheme with all linear second-order difference stencils, which can lead to spurious numerical oscillations. These oscillations are undesirable for the present application where the underlying governing equations are already known to be unstable.

To combine increased accuracy and enhanced stability, a nonlinear flux-limiter is used for the extrapolated variables, which implies some physical interpretation in determining the direction of the "wind" or flow, here given by the sign of u. The general-piecewise limiter (GPL) of Waterson and Deconinck [8] is used here because it is relatively simple and can easily be tuned to produce a variety of popular schemes.

The structure of the flux limiter for the right face value of the α variable in Eq. (14) is

$$\hat{\alpha}_R = \alpha_c + \delta x_c \Psi(r)\left(\frac{\partial\alpha}{\partial x}\right)_{UD}, \tag{16}$$

where r is the gradient ratio defined by

$$r = \left(\frac{\partial\alpha}{\partial x}\right)_{CD} \Big/ \left(\frac{\partial\alpha}{\partial x}\right)_{UD}. \tag{17}$$

The subscripts CD and UD indicate the center and upwind differences for the location R. In the present work, a uniform mesh will always be applied so that Eq. (17) simplifies to

$$r = \frac{\alpha_{c+1} - \alpha_c}{\alpha_c - \alpha_{c-1}} \tag{18}$$

for positive flow, i.e., $u > 0$. The function $\Psi(r)$ is the flux limiter, and the GPL scheme is given by

$$\Psi(r) = \max\left[0, \min\left\{(2+a)r, \frac{1}{2}(1+k)r + \frac{1}{2}(1-k)r, M\right\}\right]. \tag{19}$$

The left values as well as the extrapolated variables of Eq. (15) are found in the same manner with the neighboring cell locations shifted appropriately.

The GPL limiter of Eq. (19) can be tuned to give several classical flux limiters, e.g., the minmod scheme of Roe [9] by setting $a = k = -1$ and $M = 1$ and the MUSCL scheme of van Leer [10] by setting $a = k = 0$ and $M = 2$. In this work, the GPL scheme will be set to $a = 0$, $k = 1/2$ and $M = 4$, which results in the converted normalized variable (NV) SMART scheme of Gaskell and Lau [11]. The SMART scheme performed better for discontinuous solution data and was also slightly higher than second order accurate for smooth data [8]. The SMART scheme has been selected because it is known in advance that the KY equations produce solutions with shock-like structures, i.e., small regions of space where the solution changes rapidly. It should be noted that unlike minmod and MUSCL, the limiter form of SMART is not exactly total variation diminishing (TVD). However, it is nonoscillatory in its original NV form, which has a rough equivalence to TVD [12]. The GPL can also be tuned to a

few other schemes of less practical interest outlined by Waterson and Deconinck [8]. Additionally, by setting the limiter to the constants $\Psi(r) = 0$ or $\Psi(r) = 1$, the FOU and center difference schemes are recovered, respectively.

3.3. Time advancement

For the time advancement, a Runge–Kutta method is selected. Rather than the standard fourth-order method that is often used, a strong stability preserving (SSP) third-order method is used in keeping with the theme of increased numerical stability. Essentially, SSP schemes are the temporal equivalent to TDV spatial discretizations. The optimal third order, three stage (3–3) SSP Runge–Kutta method of Gottlieb and Shu [13] is used to approximate Eq. (13), which is defined by

$$\begin{aligned}
\phi^{(1)} &= \phi^n + \Delta t \cdot f_\phi(\alpha^n, u^n, t^n) \\
\phi^{(2)} &= \frac{1}{4}\phi^{(1)} + \frac{3}{4}\phi^n + \frac{1}{4}\Delta t \cdot f_\phi\left(\alpha^{(1)}, u^{(1)}, t^{n+1}\right) \\
\phi^{n+1} &= \frac{2}{3}\phi^{(2)} + \frac{1}{3}\phi^n + \frac{2}{3}\Delta t \cdot f_\phi\left(\alpha^{(2)}, u^{(2)}, t^{n+1/2}\right)
\end{aligned} \tag{20}$$

where Δt is the time step size between levels n and $n+1$, and the difference functions are given in Eqs. (14) and (15).

This method is the most widely used SSP Runge–Kutta scheme because it is relatively inexpensive computationally and has a Courant–Fredrichs–Lewy (CFL) criterion of unity [14]. Combining the CFL condition with the restriction due to the explicit treatment of the diffusion terms, the resulting heuristic numerical stability constraint is

$$\Delta t \leqslant \min\left[\frac{\Delta x^2}{2\nu}, \frac{2\nu}{u_\infty^2}\right], \tag{21}$$

assuming $\varepsilon = \nu$. The infinity subscript indicates the largest absolute value $u_\infty = \max|u_j|$ in the domain.

In the end, the global method is a mix of second-order accurate centered differences, fractional-order flux limited differences and a third-order time marching scheme. The total accuracy of the combined scheme is as yet unknown, although one might expect it to fall somewhere between second and third-order accuracy, the bounding upper and lower limits of the individual components. To answer this question and to determine if the resulting code has implemented these algorithms correctly, Section 4 will look at the problem of code verification.

4. Code verification

4.1. Overview

The numerical method described in Section 3 to solve the KY equations was made into a computer code using the Fortran programming language. As with any newly developed code, verification exercises should be performed. In general, verification is divided into two components: code verification and solution (or calculation) verification [15–18]. Code verification is the process of determining if the numerical algorithms were implemented correctly [17,18], which is the focus of Section 4.2, while solution verification addresses quantifying the numerical error of given solution, which is discussed in Section 5 and then again in Section 7.

4.2. Method of manufactured solutions

The simplest way to test the code's correctness (errors or bugs) and accuracy (observed convergence rate) is to compare a numerical solution to a known exact analytical solution. Unfortunately, the KY equations have no known solution that is sufficiently complex to exercise all of the terms. Certainly $\alpha(x, t) = 0$ and $u(x, t) = A$, where A is any constant, is a solution to Eqs. (1) and (2), but this solution will provide no useful information for assessing the accuracy of the code (although such trivial solutions may be useful for checking the correctness of the code, i.e., debugging). Fortunately, this problem has a clever remedy: simply manufacture a solution without being concerned about whether it exactly satisfies the governing PDEs. Then, if the manufactured solution does not exactly satisfy the governing PDEs, it is relatively straightforward to determine the residual source term that would modify the equations to make the manufactured solution an exact solution. This approach is often referred to as the method of manufactured solutions (MMS).

To begin, it helps to write of the KY equations as a pair of operators:

$$\mathcal{L}_\alpha(\alpha, u) = \frac{\partial \alpha}{\partial t} + u\frac{\partial \alpha}{\partial x} + \left(1 + \frac{\alpha}{2}\right)\frac{\partial u}{\partial x} - \varepsilon\frac{\partial^2 \alpha}{\partial x^2} + 2\alpha, \tag{22}$$

and

$$\mathcal{L}_u(\alpha, u) = \frac{\partial u}{\partial t} + u\frac{\partial u}{\partial x} - C\frac{\partial \alpha}{\partial x} - \mu\frac{\partial^2 u}{\partial x^2}. \tag{23}$$

Then, in operator form, the KY equations become $\mathcal{L}_\alpha(\alpha,u)=\mathcal{L}_u(\alpha,u)=0$ for some $\alpha(x,t)$ and $u(x,t)$ that are exact solutions to Eqs. (1), (2). Following Roach [15], traveling waves are selected for the manufactured solutions:

$$\begin{aligned}\tilde{\alpha}&=2+0.5\sin[\tilde{\kappa}(x-\tilde{c}t)]\\ \tilde{u}&=1+0.5\sin[\tilde{\kappa}(x-\tilde{c}t)].\end{aligned}\tag{24}$$

The manufactured solutions are then inserted into the operators of Eqs. (22) and (23) giving

$$\mathcal{L}_\alpha(\tilde{\alpha},\tilde{u})=\tilde{\kappa}(3/2-\tilde{c}/2)\cos[\tilde{\kappa}(x-\tilde{c}t)]+(1+\varepsilon\tilde{\kappa}^2/2)\sin[\tilde{\kappa}(x-\tilde{c}t)]+\tilde{\kappa}(3/16)\sin[2\tilde{\kappa}(x-\tilde{c}t)]+4\equiv S_\alpha(x,t)\tag{25}$$

and

$$\mathcal{L}_u(\tilde{\alpha},\tilde{u})=(\tilde{\kappa}/2)(1-\tilde{c}-C+(1/2)\sin[\tilde{\kappa}(x-\tilde{c}t)])\cos[\tilde{\kappa}(x-\tilde{c}t)]+(\nu\tilde{\kappa}^2/2)\sin[\tilde{\kappa}(x-\tilde{c}t)]\equiv S_u(x,t)\tag{26}$$

which define the necessary source terms $S_\alpha(x,t)$ and $S_u(x,t)$ for modification of the KY equations so that the manufactured solutions of Eq. (24) are exact solutions. The procedure could equivalently be called the method of manufactured equations because it is really the governing equations that are changed from their original form, $\mathcal{L}_\phi(\alpha,u)=0$, to a modified form, $\mathcal{L}_\phi(\alpha,u)=S_\phi(x,t)$, to allow the handpicked solution to be an exact solution.

The source terms defined in Eqs. (25) and (26) are used as the sources in the finite difference functions in Eqs. (14) and (15) at discrete space locations x_i or x_j and time levels t^n. The initial conditions are given by the manufactured solutions at $t=0$. Periodic boundary conditions are applied so that no special boundary values need to be determined from the manufactured solutions, but the domain or solution should be set so that there are an integer number of periods. The error between the code-calculated solution and the manufactured exact solution will be assessed with a global L_2 norm defined by

$$e_2(\phi)=\sqrt{\sum_i^N\left(\phi_i-\tilde{\phi}(x_i)\right)^2}\Bigg/\sqrt{\sum_i^N\left(\tilde{\phi}(x_i)\right)^2}.\tag{27}$$

The coarsest grid used for the MMS is $N=25$ and the nodalization is successively doubled, i.e., Δx is halved up to $N=800$. The convergence rate between a grid N and the doubled grid $2N$ is given by

$$O=\frac{\ln[e_2(\phi_{2N})/e_2(\phi_N)]}{\ln(\Delta x_{2N}/\Delta x_N)},\tag{28}$$

which gives the order of accuracy of the code for grid sizes in the vicinity of $3N/2$. In the present work, the grid refinement is always achieved by doubling the number of nodes so the denominator in Eq. (28) is simply $\ln(1/2)$. Additionally, the time step should be refined consistently with the grid, which can be problematic because the time step is restricted by Δx^2 for small enough Δx. For each case, the ratio $r_\Delta=\Delta t/\Delta x$ is set to a constant value so that the numerical stability condition of Eq. (21) is satisfied for all grids.

4.3. Diverging case

To begin, the simplest waveform is selected, i.e., $\tilde{\kappa}=\tilde{c}=1$ in Eq. (24), so that the solution is 2π-periodic in space and time. The domain is given by $x\in[-\pi,\pi]$, and the error will be assessed at $t=2\pi$ to give one period in both space and time. The time step for each grid is set from $r_\Delta=0.0125$. As may be somewhat expected, the MMS does not work, and the calculated solution diverges from the manufactured solution. The traditional refinement plot or table is not shown because they offer little information. The important factor to demonstrate is not simply that the solution diverges but how it diverges.

The error for each variable is shown in Fig. 3 as a function of time for four different grids. The two coarsest grids have been left off of Fig. 3 because the numerical viscosity is of the same order as the viscosity of the system, i.e., $O(\Delta x^2)\approx O(\nu)$. The straight line in Fig. 3 beyond the finest grid is $e^{\omega_c(t-t^*)}$ with ω_c calculated using the average α of the exact solution and t^* is an arbitrary constant. This result shows that, for each case, there is an initial transient period after which the error grows exponentially and approximately uniformly at the critical growth rate. Beyond this period, the solution either diverges to infinity (an excursion) or reaches an asymptotic value. A discussion of the different behaviors is reserved until Section 7.

Fig. 3 is able to show that, while the MMS did not work, it failed in a way that was predicted by the linear stability analysis in Section 2.2. Error is introduced to the calculation through two primary ways: round-off error in the finite precision representation of the source terms and truncation error by the finite difference representation of the differential equations. While these errors are initially very small, the linear stability analysis predicts that even infinitesimally small perturbations will grow exponentially in time. Therefore, some adjustments are needed to proceed with the code verification.

4.4. Converging case

The most obvious change is to make the system hyperbolic by adjusting either the system or the manufactured solution. This approach was tested by setting $C=-1$, which makes the system hyperbolic for the manufactured solution of the previous section, and convergence was indeed observed. However, this method of code verification raises several concerns, namely that such an approach may not be applicable to other similar models, e.g., the 1-D two-fluid model.

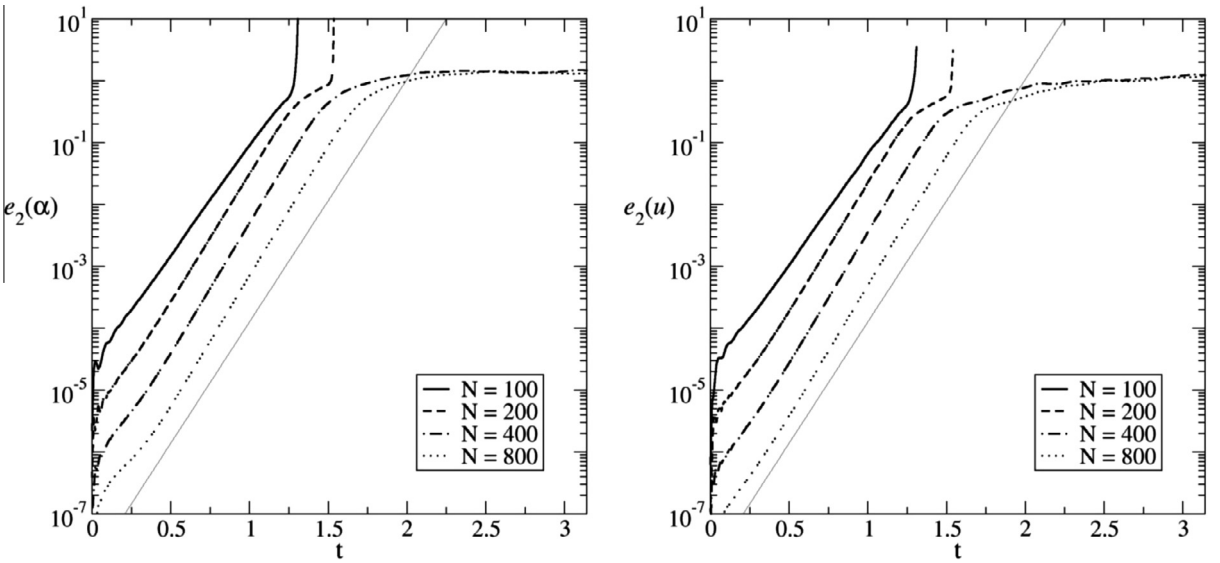

Fig. 3. Divergence from the exact solution for the case $x \in [-\pi, \pi]$. The straight line shows the average critical growth rate predicted from linear theory.

Without altering the form of the equations or the solution, there is one other option available: shrink the geometry of the problem so that domain simply cannot contain wavelengths with positive growth rates, i.e., $L \leqslant \lambda_0$. Using the maximum value of α in the manufactured solution, the maximum cut-off wavenumber is $\kappa_0 = 20\sqrt{2.15} \cong 29.3$ or $\ell_0 \cong 2\pi/29.3$. Therefore, the domain will be reduced to $x \in [-\pi/30, \pi/30]$ so that the maximum possible wavelength is less than λ_0 and linear growth should not be possible. The wavenumber of the manufactured solution is modified to fit the new domain, $\tilde{\kappa} = 30$, while the previous wave speed is retained, $\tilde{c} = 1$, so that the error is still assessed in one temporal period, $t = 2\pi$. The time step for each grid is set from $r_\Delta = 0.004$.

Now the error is reduced as the grid is refined. The error for each grid is shown in Table 1, and the convergent behavior is shown in Fig. 4. The convergence rate between two grids is also given in Table 1, which shows that the order of accuracy of the method is slightly better than second order. There is a noticeable convergence of the rate of convergence, which was also reported by others using the MMS [19]. For the coarsest grids, the refinement brings almost third-order accuracy, which is shown in Fig. 4 as the steeper initial line. However, as the grid is refined further, the order of accuracy is reduced to near second-order, which is also shown in Fig. 4.

Using such a small domain may not be physically relevant for some models, but this problem is not a concern of code verification. This approach provides a method to further distinguish ill-posed models from regularized models because, for an ill-posed model, there will be no domain where the MMS is applicable. Lastly, it should be noted that we are still left wondering whether the numerical method (and really any time marching scheme) is appropriate for this type of problem, but this issue is not really a question for the MMS or code verification in general. With code verification, one only wants to be sure the code is working correctly, which has been shown.

5. Solution verification

5.1. Comparison with the Kreiss–Ystrom solution

The verified code may now be used to solve the KY Eqs. (1) and (2). The first and most obvious test is to simulate the original problem of Kreiss and Ystrom [1] and compare with their results. The initial conditions are Gaussians of different

Table 1
Error for each grid and the convergence rate between two successive grids for the case $x \in [-\pi/30, \pi/30]$.

N	α		u	
	e_2	O	e_2	O
25	5.860E−02	–	5.187E−02	–
50	8.345E−03	2.81	6.568E−03	2.98
100	1.363E−03	2.61	9.103E−04	2.85
200	2.652E−04	2.36	1.501E−04	2.60
400	5.817E−05	2.19	2.925E−05	2.36
800	1.363E−05	2.09	6.410E−06	2.19

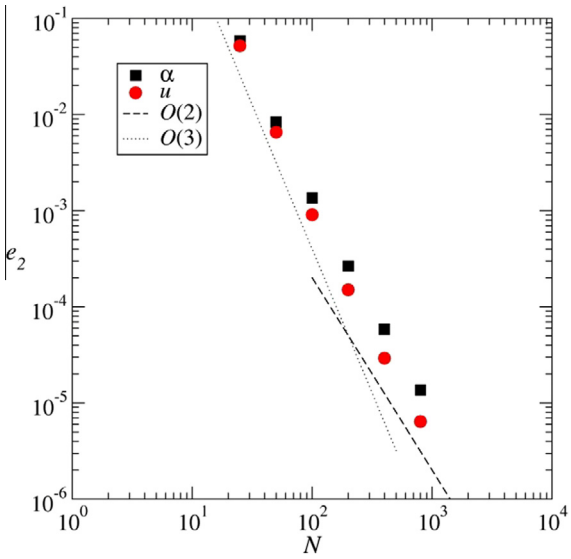

Fig. 4. Convergence rates for the second MMS case $x \in [-\pi/30, \pi/30]$.

widths defined by $\alpha_0 = e^{-2x^2}$ and $u_0 = e^{-4x^2}$, which are periodic about the origin. The domain is $x \in [-\pi, \pi]$, the grid is divided into $N = 512$ uniform nodes and the time step is set to $\Delta t = 0.0002$. Comparisons to the published solutions are given Fig. 5.

From the initial condition to $t = 1$, the two numerical solutions are nearly indistinguishable. Even up to a time of $t = 4$, only relatively minor differences are observed. However, at the last time, $t = 40$, the two solutions are entirely different; even though the features of the two solutions are similar.

On the surface, this difference does not appear to be troublesome. After all, the numerical solution of Kreiss and Ystrom [1] was obtained using a higher resolution pseudo-spectral method, which was shown to be fully converged for up to $t = 8$. Showing that the numerical solution is fully converged or grid independent ensures that the numerical solution is an accurate approximation to the system of PDEs. Quantifying the accuracy of a given solution is the process of solution verification or numerical error estimation [18]. Solution verification can take on several forms, ranging from estimating the exact solution from a series of numerical solutions using the method of Richardson [20] to a more engineering approach of refining the grid until two successive solutions become (relatively) indistinguishable.

The exact method for solution verification seems to be irrelevant here because any method is predicated on the simple fact that the solutions on successive grids are in fact converging. The solutions at $t = 40$ are shown in Fig. 6 for successively doubled grids from $N = 512$ to $N = 4096$. It can be observed that even with nearly an order of magnitude more grid points, the solutions are different from that reported by Kreiss and Ystrom [1] and equally different from each other. While the features of the solutions are again quite similar, what is so unsettling about Fig. 6 is that none of these features seem to be changing systematically with the grid refinement: amplitudes are not increasing, slopes are not steepening, frequencies are not increasing, waves are not translating (i.e., from dispersive errors). Each solution appears to be a different snapshot of a single grid, or at least similar grids, at different times. Such a fundamental lack of convergence renders any type solution verification impossible, at least for this code, in this time domain.

5.2. Sensitivity to initial conditions

While it may be impossible, or at least impractical, to complete the solution verification via error estimation at this point, it is important to understand why this lack of convergence is happening. The answer is similar to what happened with the MMS on the first, larger grid: very small errors are growing exponentially. Although each case starts with the same initial condition (or at least as similar as can be represented on a different grid), the truncation errors are different for each grid. This can be shown clearly using a single grid ($N = 512$) and introducing a very small perturbation and tracking the evolution of this difference in time.

The initial conditions will now be defined by $\tilde{\alpha}_0 = e^{-(2+\delta_\alpha)x^2}$ and $\tilde{u}_0 = e^{-(4+\delta_u)x^2}$ so that perturbations are now included in the widths of the Gaussians. The original, unperturbed case is recovered by $\delta_\alpha = \delta_u = 0$. Following Sprott [21,23], the magnitude of the perturbations will be taken to be on the order of the square root of the precision of the floating point numbers being used, double precision in this case, so that $|\delta_\alpha| = |\delta_u| = \delta_0 = 10^{-8}$. Perturbations to the initial condition will be solved in time simultaneously with the unperturbed case. The difference will be treated as an error and quantified with the L_2 norm given in Eq. (27). Four different perturbations will be considered, each with the magnitude given by δ_0 and the signs of $(\delta_\alpha, \delta_u)$ given by (+ +), (+ −), (− +) and (− −).

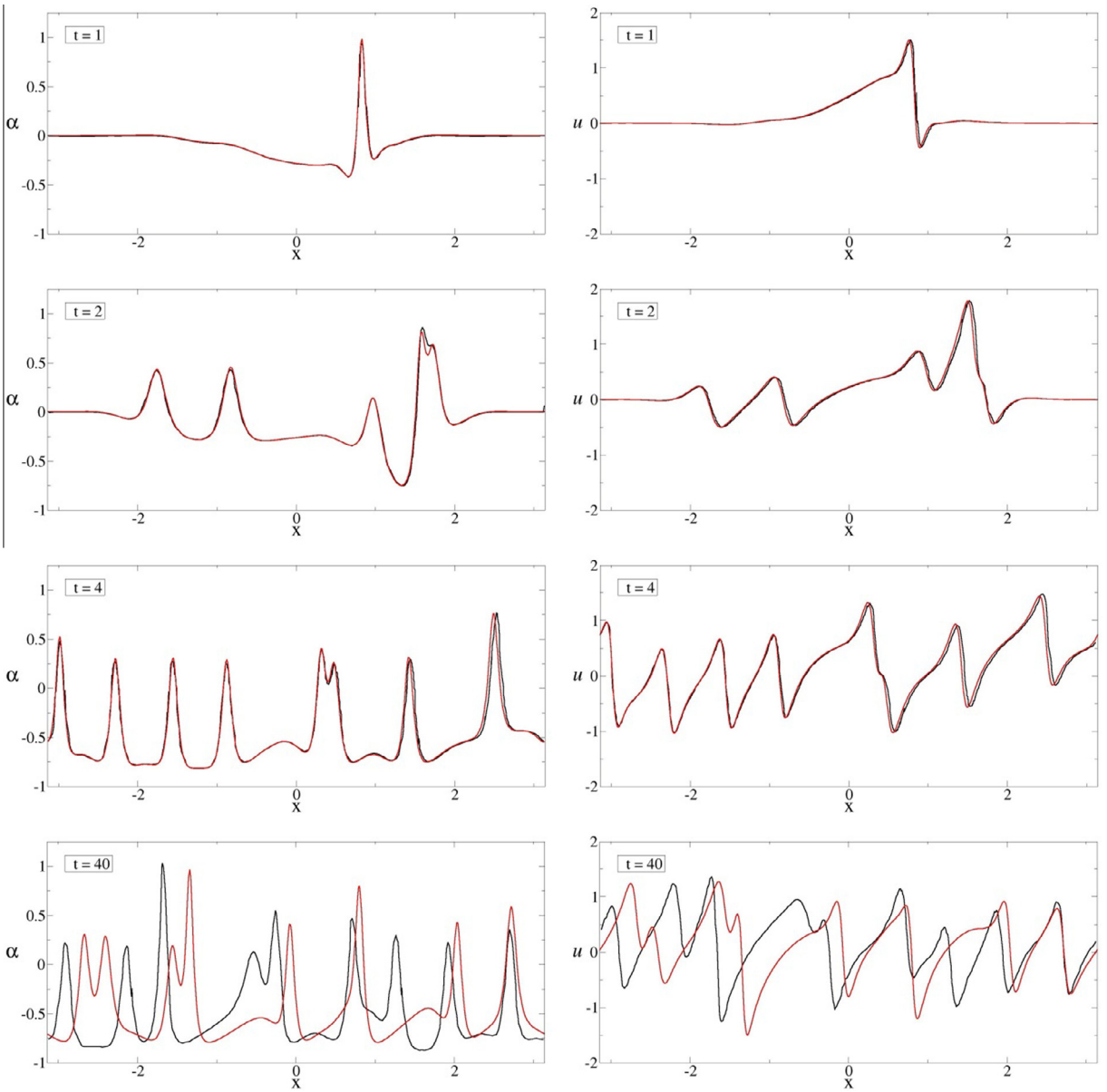

Fig. 5. Numerical solution to the KY equations (red) compared to the original results [1] (black). (For interpretation of the references to colour in this figure legend, the reader is referred to the web version of this article.)

Because the behavior of each is qualitatively similar, the norms of the variables are summed in Fig. 7 to give the total error. Except for in the very small time domain, the solutions diverge much more slowly than $e^{\omega_c(t-t^*)}$, which was observed in the first MMS case. Instead, each perturbation solution is diverging from the unperturbed case approximately at a rate of $e^{0.38(t-t^*)}$ shown by the dashed lines in Fig. 7 (the value of 0.38 will become clear in Section 6.1). The slowed divergence rate is a result of the nonlinearity and was also observed by the original authors [1]. While the logarithm of this growth rate is about an order of magnitude less than predicted by linear theory, the divergence eventually leads to entirely different solutions when the total error saturates around $t = 50$, which shows that the solutions are very sensitive to the initial conditions, i.e., small changes in the initial state can eventually lead to drastic changes in later states, which is an indication of chaos and was first termed the *butterfly effect* by Lorenz. The idea of chaos in the KY equations will be explored in some detail in the following section.

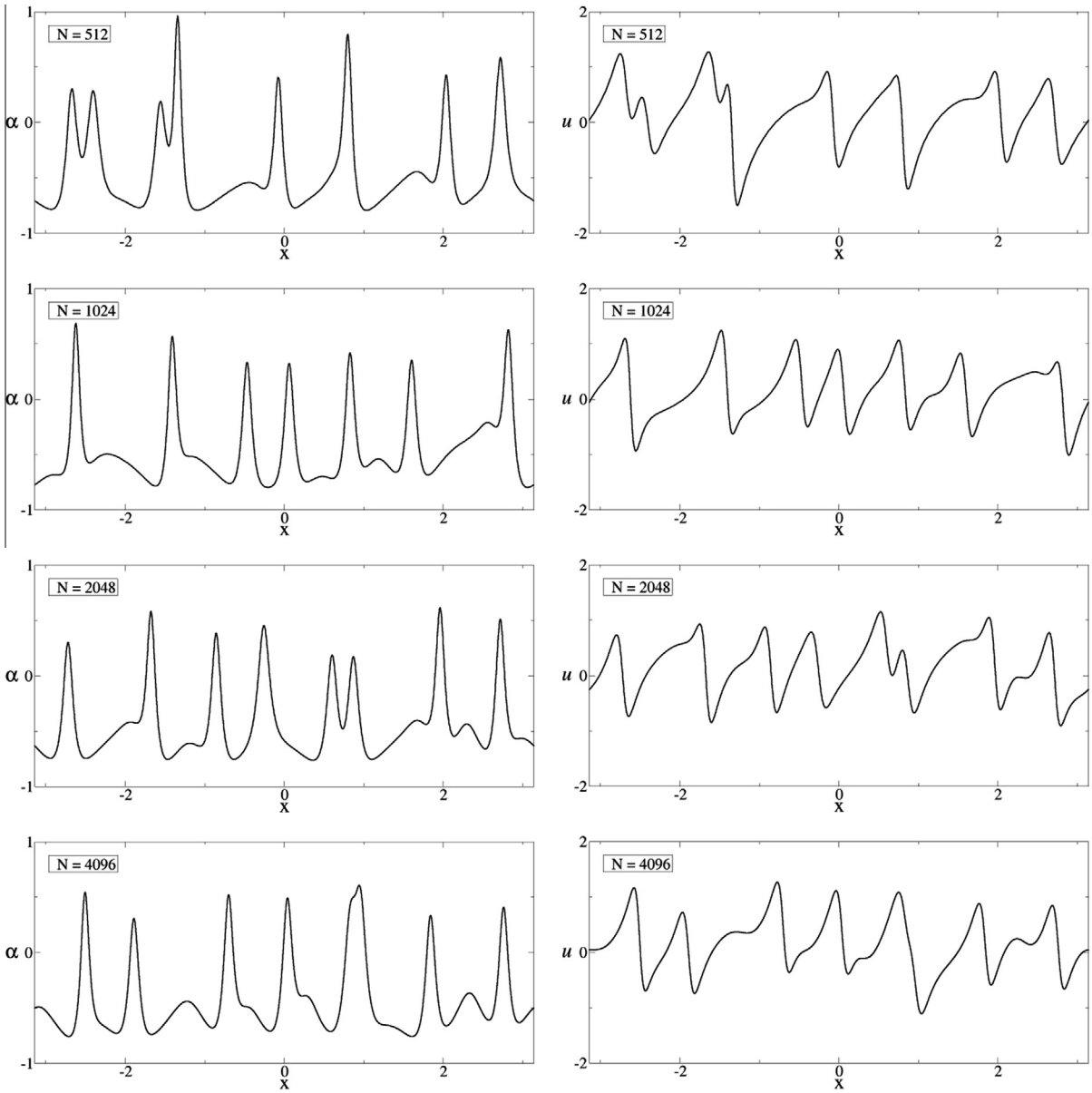

Fig. 6. Numerical solutions of the KY equations at $t = 40$ on four different grids.

6. Chaos and bounded nonlinear waves

6.1. Lyapunov exponent

While there may not be a formal mathematical proof of chaos, a standard test and the best way to quantify the chaos is with the Lyapunov exponents [21], specifically the largest Lyapunov exponent (LLE). For a finite dimensional system of ODEs, there are as many exponents as there are dimensions. For a PDE or system of PDEs, the number of exponents is infinite. Luckily, the calculation of the largest Lyapunov exponent is tractable and its sign signifies whether a system is chaotic and its magnitude determines the degree of chaos. In many respects, the LLE is to nonlinear analysis as the growth rate is to linear analysis.

More specifically, the LLE calculates the average rate at which two nearby states converge to or diverge from one another. The LLE is defined by

$$\mathrm{LLE} = \lim_{t\to\infty}\lim_{d\to 0}\frac{1}{t}\ln\frac{d(t)}{d_0}, \tag{29}$$

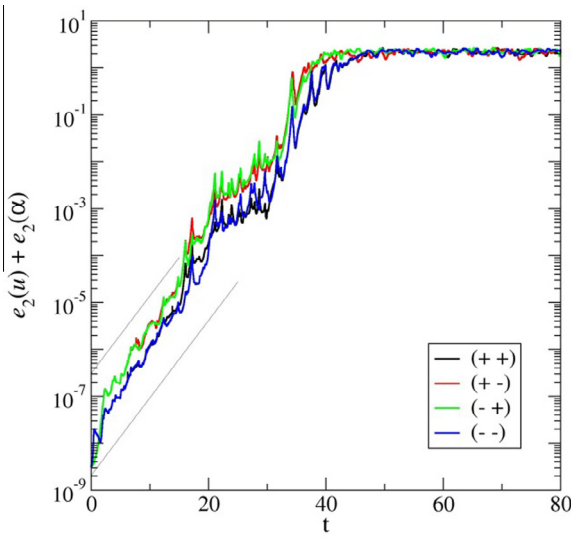

Fig. 7. The divergence of four solutions with slightly perturbed initial conditions compared to the unperturbed case.

where d_0 is some initial separation between two trajectories (solutions) and $d(t)$ is the separation at some later time. Note that d_0 is not necessarily introduced at $t = 0$. A positive LLE indicates that the solutions are diverging and that the system is chaotic. The magnitude of the LLE approximates the rate at which the predictability of the system is lost [21]. If the solutions are diverging, the limits in Eq. (29) seem to contradict one another. Therefore, in practice, the two trajectories are never allowed to diverge too far from one another before being reset. The LLE is calculated and averaged over many periods to obtain satisfactory statistics.

The system of PDEs is treated as a $2N$-dimensional system of ODEs for which the general procedure is relatively straightforward. First, the solution is solved for a period of time to allow any transients to settle out, which is particularly important because the condition that guarantees convergence of finite time Lyapunov exponents to the global Lyapunov exponents is that the underlying system has an invariant attractor [22]. Then, at a specified time, a minor perturbation is introduced and this second solution is also followed. For many short intervals of time, the two solutions are solved and the perturbed solution is compared to the original unperturbed solution to determine the evolution of the separation. Then, the perturbed solution is renormalized against unperturbed solutions so that the difference between the two solutions does not grow too large and the procedure is repeated.

The perturbation should be introduced in the direction of the maximum divergence, which may not be easy to evaluate. Therefore, a simple, general perturbation is introduced and the system is given a period of time, here 1000 time units, for the perturbation to orient in the direction of maximum expansion [21]. The first imposed perturbation is specified as $\tilde{\alpha} = \alpha - \mathrm{sgn}(x)\delta_0$ and $\tilde{u} = u + \mathrm{sgn}(x)\delta_0$ with tilde overbars again signifying the perturbed solution. It should be noted that the perturbation slightly breaks periodicity equally at the edge and center of the domain, which is so that there is no integral change to the perturbed solution which would slightly alter its equilibrium position. The magnitude of the separation in both variables at each spatial location, i.e., in each of the $2N$-dimensions, is the same as that used previously, $\delta_0 = 10^{-8}$. The total separation is given by the $2N$-dimensional Euclidean norm

$$d_k = \sqrt{\sum_i^N (\tilde{\alpha}_i - \alpha_i)^2 + (\tilde{u}_i - u_i)^2}. \tag{30}$$

The subscript k is used to indicate that the LLE calculation number is in general not the same as the iteration number n unless the perturbation is introduced at time zero. The initial separation is then $d_0 = \sqrt{2N}\delta_0$.

Following Sprott [21,23], the LLE is calculated after each iteration so that the separation does not become too large and then the perturbation is readjusted. The perturbation is adjusted so that the perturbed orbit is preserved while renormalizing the net separation to be d_0 again, i.e.,

$$\tilde{\phi}_i = \phi_i + d_0(\tilde{\phi}_i - \phi)/d_k. \tag{31}$$

Finally, the LLE is given by the logarithm of the ratio of the net separation at time k to $k-1$, and because the starting separation is always renormalized to the initial separation, it is simply

$$\mathrm{LLE} = \frac{1}{k}\sum_{k=1}^{k\to\infty} \ln\frac{d_k}{d_0}. \tag{32}$$

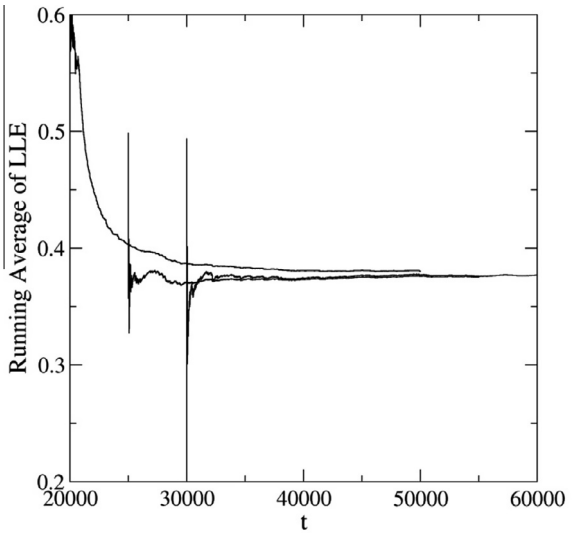

Fig. 8. Running average of three LLE calculations started at different times.

Generally, this calculation needs to be performed for very long periods of time to determine the LLE with a high degree of precision. Here, however, the primary concern is simply determining whether the LLE is positive and obtaining an approximate value.

The LLE calculation was started at three different times: $t = 2 \cdot 10^4$, $2.5 \cdot 10^4$ and $3 \cdot 10^4$. Each calculation started with the initial perturbation described previously, which was introduced 10^3 time units before the calculation began to allow the perturbed solution to orient itself in the direction of maximum expansion. Each calculation is performed for $3 \cdot 10^4$ time units. The running average of each calculation is shown in Fig. 8. Even at a time of $t = 2 \cdot 10^4$, there is still some of the initial transient in the solution, which is apparent in the running average of the first LLE calculation. However, the average eventually settles down when the number of samples becomes large and agrees with the other two calculations. Taking an average of the three final values and using $1/\sqrt{f \cdot t}$ to estimate the order of accuracy (where f is the characteristic frequency and t is the calculation time), the LLE is determined to be 0.38 ± 0.05. This measure quantifies the reduced rate of the divergence of the solutions with the slightly perturbed initial conditions, refer back to Fig. 7.

6.2. Fractal dimension

Beyond showing that the LLE is positive, the second most important sign of chaos is that of a fractal dimension of the dynamics. The fractal dimension measures the "strangeness" of the attractor [24–26]. There are several techniques to measure the dimensionality, each of which produces slightly different results. Here, the correlation dimension is used because it is easier to calculate than other measures and converges rapidly [21,24,27].

In general, the correlation dimension is calculated by shrinking a hypersphere in d_E -dimensional space of radius r and counting the number of points inside the hypersphere, which is given by the correlation sum, $C(r)$. As the total number of points tends to infinity, the correlation sum converges to the correlation integral and behaves as

$$C(r) \propto r^{d_C}, \tag{33}$$

as the radius tends to zero. Therefore, on a logarithmic plot, the slope of $C(r)$ vs. r gives the correlation dimension d_C.

Part of the challenge is that there are simultaneously two unknowns: the correlation dimension and the phase-space dimension in which the fractal dimension should be calculated. For instance, a line has $d_C = 1$ whether it is constructed in 2-D space, 3-D space or any higher dimension. The dimension of the construction is called the embedded dimension, d_E. In this case, the dimensionality of the problem is infinite or $2N$ when the PDEs are solved with the finite difference scheme discretizing the spatial domain in N segments. However, it may not be necessary to use all $2N$ variables to capture the dynamics of the problem. Therefore, the correlation dimension is first calculated with an embedded dimension of one, which is almost surely insufficient, and then repeated several times, each time increasing the imbedding dimension. At some point, the correlation dimension will stop changing, giving both and the minimum embedded dimension.

To create the phase-space, the u variable is recorded at d_E equidistant positions in the spatial domain every 250 iterations in the time domain $t = 2.5 \cdot 10^4$ to $6.5 \cdot 10^4$. The left of Fig. 9 shows $C(r)$ in the logarithmic scale for d_E from one to nine. The successive slopes correspond to d_C, which are plotted on the right of Fig. 9 as a function of d_E. The correlation dimension saturates at $d_C \cong 2.8$ with a minimum embedded dimension of $d_E = 6$, which indicates that in principle the dynamics of the system may be modeled without overlapping using only six state variables [27].

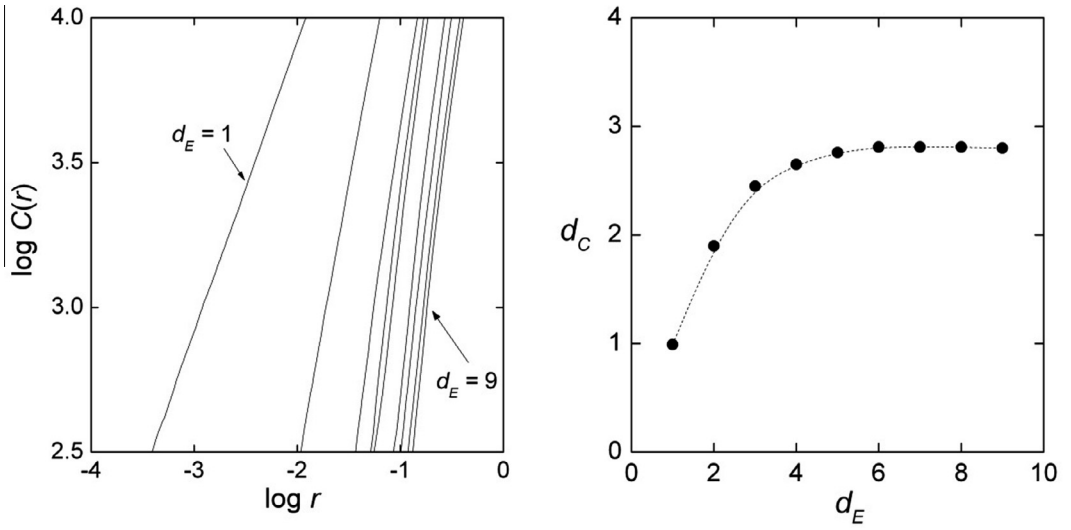

Fig. 9. Calculation of the correlation dimension as a function of the embedded dimension.

6.3. The route to chaos

Each of the two previous sections were devoted to the calculation of a single number, namely the LLE in Section 6.1 and the fractal dimension in 6.2. Here, the emphasis will be more qualitative than quantitative in exploring how the equations evolve from stable to chaotic states. For this study, the coefficient C in the KY Eqs. (1) and (2) will be the control parameter, which seems to be the best choice because it was already shown to be directly related to the critical growth rate from the linear stability analysis. Accordingly, the dynamics of the system are explored by varying C starting with negative (stable) values and progressively increasing it to positive (unstable) values. All of the tests were performed with the viscosities, boundary and initial conditions and numerical grid ($N = 512$ and $\Delta t = 0.0002$) used previously in Section 5.1. The equations are solved numerically letting the initial transient pass (in some cases up to $t = 2.5 \cdot 10^4$ as was observed in Fig. 7) and then the long-term dynamics, either stable or unstable, are analyzed.

The dynamics are visualized by the trajectory of the state variables at the center of the domain, labeled α_0 and u_0 in the following figures. With this phase-space construction it is easy to see how the variables are approaching the attractor, i.e., the equilibrium position, which corresponds to the constant uniform values $\alpha = 0$ and $u \approx 0.141$. The former is forced to zero by the dissipative sink in Eq. (1) and the latter is a consequence of the periodic boundary conditions, which ensure that the integral conservation of u is given by $\int_{-\pi}^{\pi} e^{-4x^2} dx = \sqrt{\pi/4}\mathrm{Erf}[2\pi] \approx 0.141$ in the limit $N \to \infty$. In addition, a third dimension is

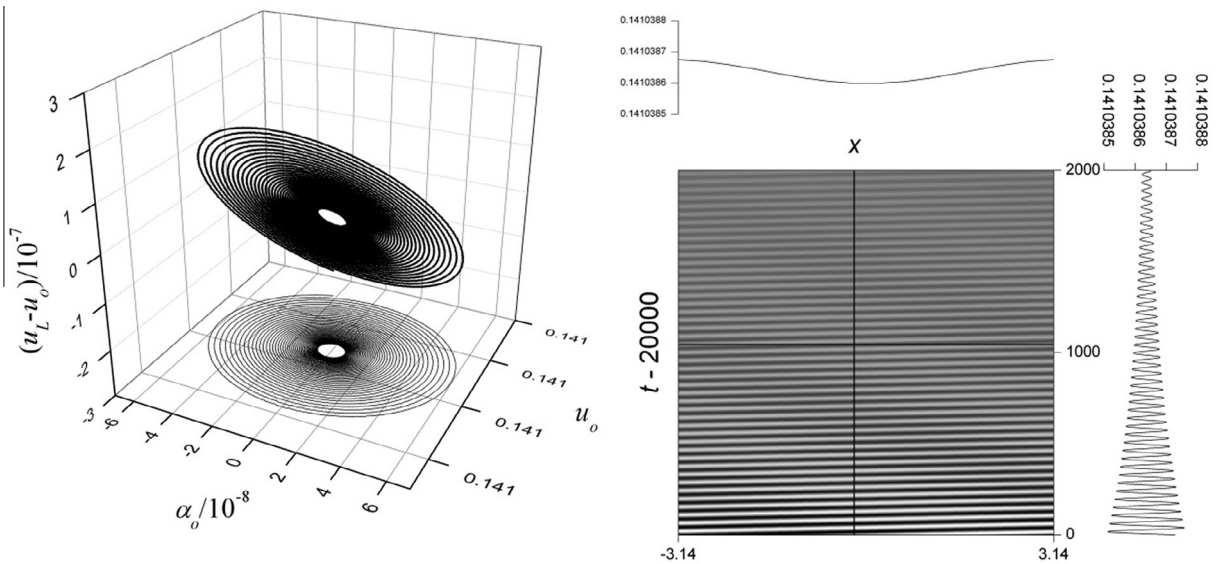

Fig. 10. Phase-space and grey scale map of $u(x, t)$ for $C = 0.102$ showing the asymptotic stability of the system.

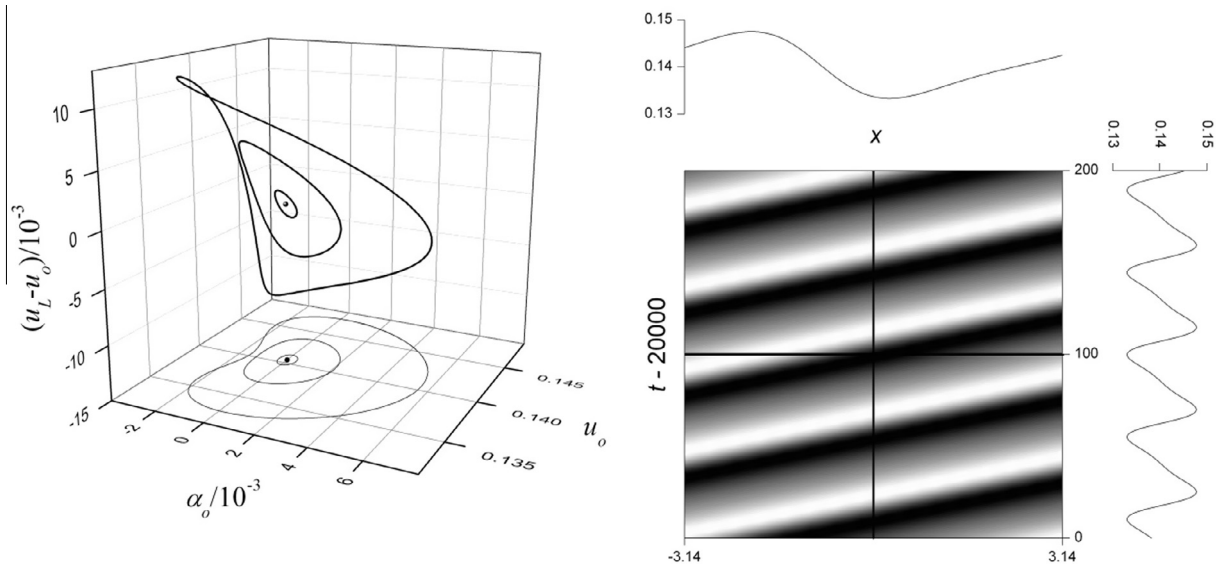

Fig. 11. Phase-space for $C = 0.102$, 0.1025, 0.103 and 0.105 and grey-scale map of $u(x, t)$ for $C = 0.103$ showing 2π-periodic limit cycles, increasing in amplitude with increasing C.

added to the phase-space to help unfold some of the dynamics, although an embedded dimension of six precludes unfolding all of the chaotic dynamics into a visualizable space in the chaotic region. The difference between u at the boundary and center of the spatial domain, $u_L - u_0$, was found to provide a useful third dimension. This variable can be used to distinguish between 2π- and π-periodic functions. Its equilibrium value is zero due to the uniform equilibrium condition.

When $C < 0$, the solution quickly approaches equilibrium, which is the expected behavior for a linearly stable hyperbolic system. When C becomes positive, the system remains linearly stable due to the diffusion, i.e., the domain is smaller than the cut-off wavelength. There is a critical value of C when the size of the domain (and therefore the largest possible wavelength) is equal to the cut-off wavelength, $\lambda_0(C^*) = L$. The present case, $L = 2\pi$, $\nu = 0.05$ and using the equilibrium value $\alpha = 0$, gives $C^* = 0.1025$. The decay rate of the approach to the equilibrium position slows dramatically as C approaches C^*. This behavior is shown in Fig. 10 for $C = 0.102$. The left hand side of the figure shows the slow spiral of the state variables into the attractor and the right hand side shows a brief map of the spatiotemporal evolution.

As C increases slightly beyond C^*, the steady state of the system becomes unstable and a 2π-periodic traveling wave is developed. The wave travels at a constant speed, which is shown by the parallel lines in the grey-scale contour map of Fig. 11, taken after the sustained wave is reached. This behavior corresponds to a limit cycle in phase-space. The amplitude

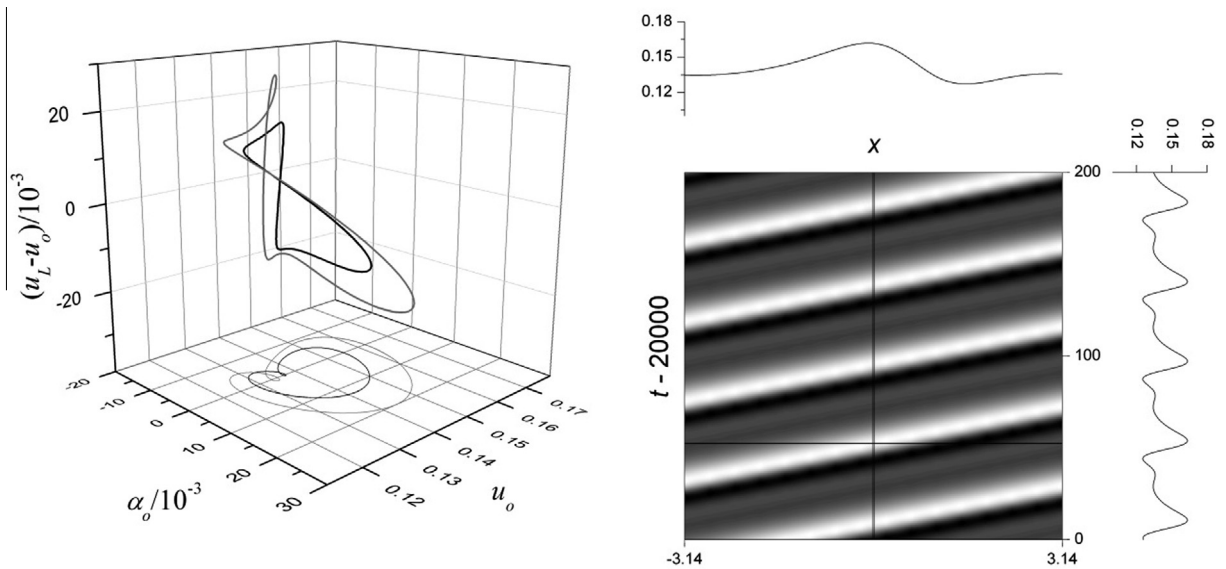

Fig. 12. Phase-space for $C = 0.107$, 0.109 and 0.111 and grey-scale map of $u(x, t)$ for $C = 0.109$, showing asymmetric 2π-periodic limit cycles, increasing in amplitude with increasing C.

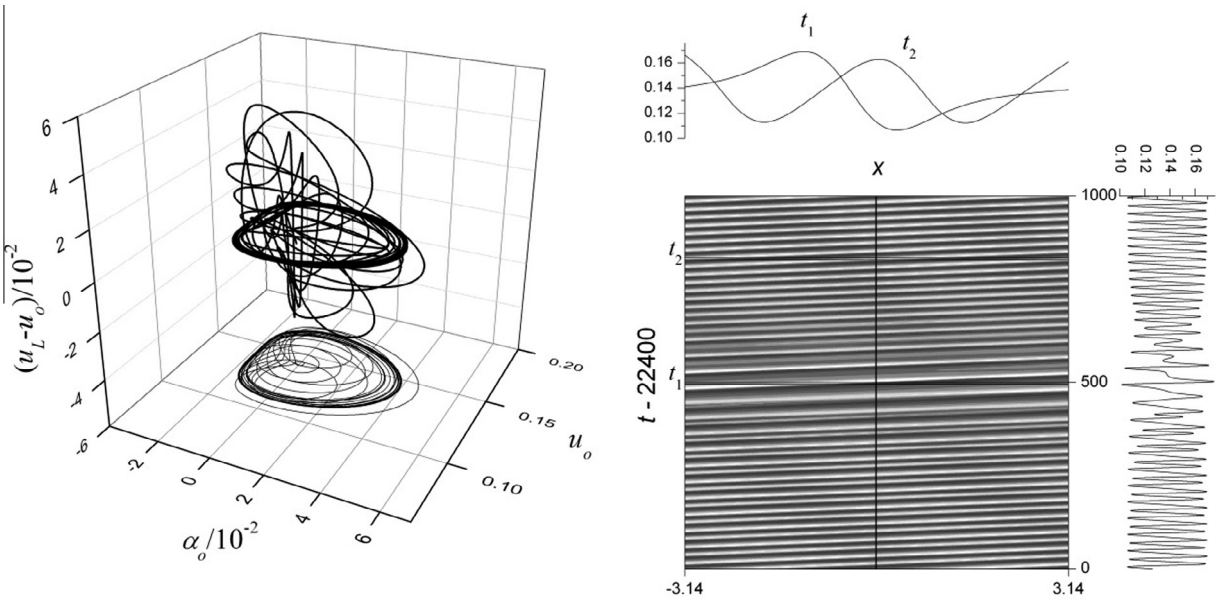

Fig. 13. Phase-space and grey-scale map of $u(x, t)$ for $C = 0.115$ showing a burst of brief, intermittent chaos surrounded by π-periodic limit cycles.

of the wave and the limit cycle grow as C increases, observed on the left of Fig. 11. Near $C = 0.104$, the limit cycle becomes deformed and begins to appear heart-shaped, as shown on the right of Fig. 11 for $C = 0.105$. Beyond $C = 0.107$, the limit cycle becomes significantly more complex with a curl in the trajectory as observed in Fig. 12. This behavior corresponds to a steepening wave front and the development a secondary wave pattern.

At $C = 0.112$, the system develops intermittency with relatively long periods of periodic, regular waves interrupted by short bursts of another wave pattern. Intermittency is one of the three basic types of bifurcations leading to chaos, along with quasiperiodic and period doubling [21]. In the phase-space it is difficult to distinguish between intermittency and chaos for a long time series of data. However, on the right of Fig. 13, the brief interruption in the temporal signal is easily recognizable.

This behavior continues up to $C = 0.116$. Between 0.116 and 0.120 another stable traveling wave appears with a wavelength of half the spatial domain. This feature can be appreciated in Fig. 14 which shows that the limit cycle is now flat in the third dimension due to the π-periodic wave which is shown above the map.

Finally, after another brief region of intermittency, the system becomes chaotic at $C = 0.125$. Fig. 15 shows a slightly more chaotic state for $C = 0.150$. For clarity, only a brief part of the trajectory in the phase-space is plotted, for the evolution is so entangled that it is difficult to visualize in this representation (actually we would need 6 axis to disentangle the chaotic trajectory). On the right of Fig. 15, the map of $u(x, t)$ shows that the regularity of the standing wave is lost, i.e., uniform amplitudes, periods, propagation speeds, etc., and the complexity of the dynamics can be observed. This chaotic state continues and increases in complexity as C increases up to the original value of one.

7. Solution verification revisited

Now that it has been demonstrated that the KY equations are chaotic, it is understandable why the results in Fig. 5 do not match the published results, at least beyond some initial time frame. While it may be impossible to reproduce the solution exactly with a different code, the question of solution verification still remains. That is, how to judge when a grid for the numerical scheme is sufficient. A new method to assess convergence is needed because, due to the positive LLE, any perturbation no matter how small, e.g., different grid, will eventually diverge. Chaos theory provides several possible options, some of which have already been discussed, namely the LLE and the fractal dimension. These measures are invariant; that is, unlike the solution as a function of time, these measures are insensitive to perturbations of the initial conditions [27]. Unfortunately, calculating these quantities for several grids is quite computationally expensive. Additionally, because it is hoped that the analysis of the KY equations will serve some guidance to the 1-D two-fluid model, calculating these quantities with physical models for physical problems may be impossible. Therefore, perhaps it is best to borrow concepts from a well-known physical model that exhibits similar spatio-temporal convergence challenges: the Navier–Stokes equations.

When the Navier–Stokes equations are solved using large eddy simulation, for a sufficiently large Reynolds number, the flow becomes turbulent and one can no longer compare the solution at a particular time as a function of the grid size. Instead, it is quite typical to assess the convergence based on the law of the wall (for internal flows), the auto-correlation function or one of the energy spectra. While these may not be so well defined for the nonphysical KY system, a common

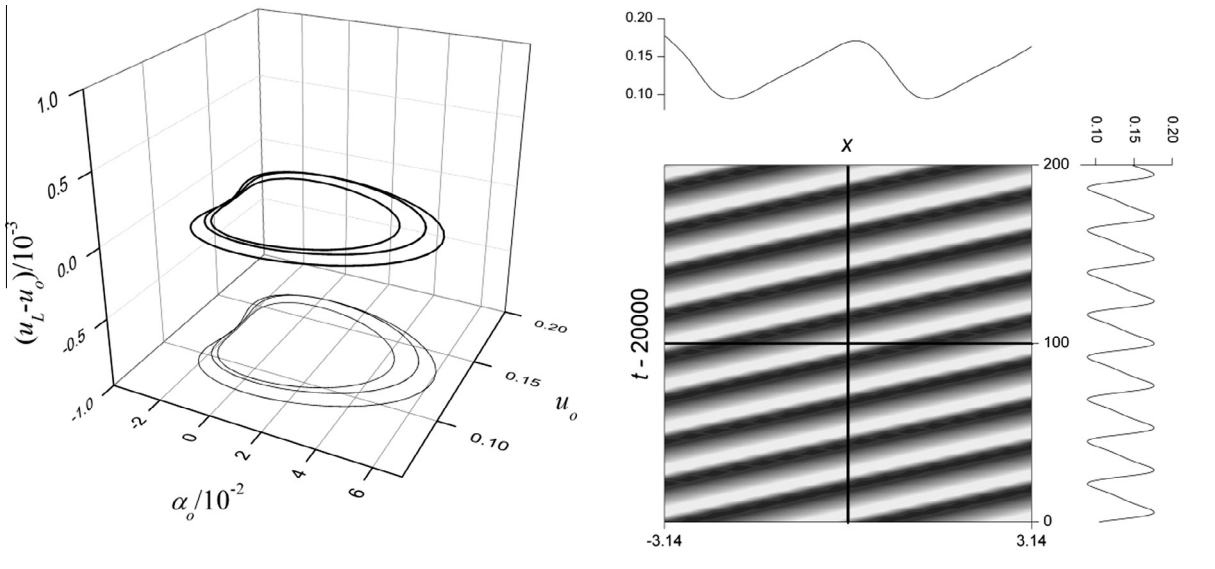

Fig. 14. Phase-space for $C = 0.116$, 0.118, and 0.120 and grey-scale map of $u(x, t)$ for C = 0.120 showing π-periodic limit cycles, increasing in amplitude with increasing C.

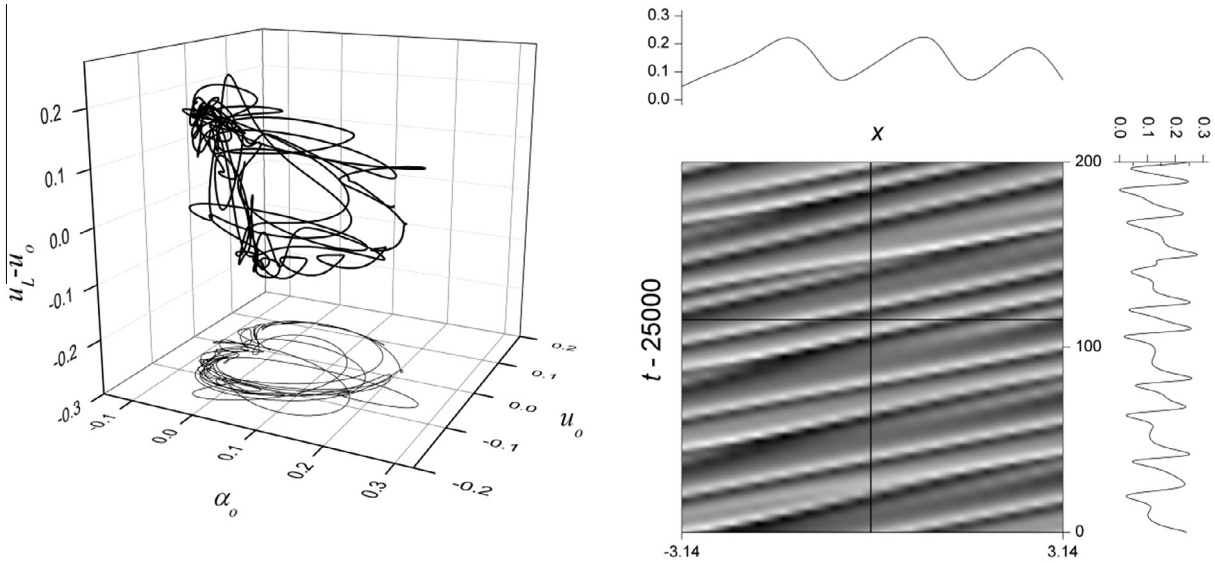

Fig. 15. Phase-space and grey-scale map of $u(x, t)$ for $C = 0.150$ showing chaotic and aperiodic behavior.

feature is that they are all averaged measures. In this case, convergence will be assessed with the average amplitude in wave space by averaging the Fourier transform of $\alpha(x) \to \alpha(\kappa)$ and $u(x) \to u(\kappa)$. The first sample is taken at $t = 4$ when the wave pattern fills the domain and 36 additional samples are taken up to $t = 40$.

The averaged amplitude spectra are shown in Fig. 16 for successively doubled grids from $N = 256$ to $N = 4096$. From here, it is up to the user to make a determination of what is "resolved enough." For the present numerical method it seems that the $N = 512$ grid is sufficiently resolved because it correctly captures 99.99% of the amplitude spectrum, i.e., from the maximum amplitude of 0.1 down to approximately 0.00001 where the numerical tail introduces significant error. In contrast, $N = 256$ only captures approximately 99% of the spectrum correctly and higher grids lose much of their potential value to the growing numerical tails. This result shows that even though the numerical method may be considered "high-resolution" compared to linear upwind methods, it is still quite coarse in the spectral domain.

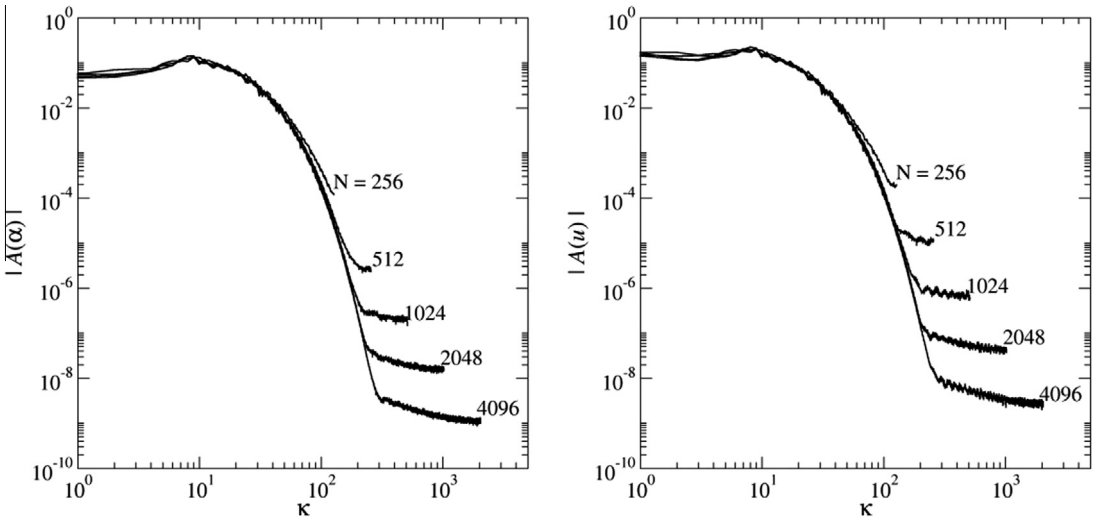

Fig. 16. Averaged power spectra of the amplitude of each variable in the time domain $t \in [4, 40]$ sampled at a frequency of 1 Hz.

At this point, it is hard not to draw a comparison between the present KY equations and the Kuramoto–Sivashinsky (KS) equation, which was physically derived to model chemical reactions [28]. In both cases, the mechanism generating the chaos is the same: energy is generated at small wavenumbers, where the model is linearly unstable, which is transferred to larger wavenumbers through shock-like structures by the nonlinearity until it reaches a sufficiently large wavenumber where the energy is dissipated by viscosity, which is the reason that truncation errors that grow exponentially will cause the same initial condition on two different grids to evolve into two different solutions, rather than just growing exponentially forever causing a numerical excursion.

Lastly, it should be noted that Fig. 16 helps explain the different behavior of the divergent MMS cases in Fig. 3. For grids with resolution less than approximately $N < 256$, the code could not calculate a solution to the KY equations. This behavior appears to be a result of not having a sufficient amount of high wavenumber nodes to dissipate the energy generated at the large scale, which is not a universal grid resolution requirement to the governing equations, but specific to the numerical method. A different scheme with better spectral resolution would likely be able to obtain a solution with less refinement. Therefore, in all of the cases presented in Fig. 3, the underlying KY equations dominated the MMS and are trying to produce solutions similar to the KY equations, but with a large modified source term. The finer grids are capable of solving this system and reach an asymptotic value for the error when a quasi-steady state is reached. However, the coarser grids simply do not resolve enough of the spectrum to dissipate the energy that is generated at the large scale, which leads to the blow up.

8. Conclusions

This work presented a detailed analysis of the two PDE system originally proposed by Kreiss and Ystrom [1]. The KY equations are conditionally ill-posed as an IBVP when the characteristics of the system are complex. A linear stability analysis was used to show the effect of higher-order viscous regularization, which parallels similar regularization methods for the 1-D two-fluid model. A simple finite-difference numerical method was used to solve the KY equations. When the code was tested with the MMS, divergence from the manufactured solution was observed and a convergence test could not be performed. It was shown that the rate of divergence was predicted nearly exactly by the critical growth rate of the linear stability analysis. Using the linear stability analysis as a guide, a smaller spatial domain was used, which was restricted to less than the minimum cut-off wavelength. The MMS did converge on the smaller domain, and a convergence test was performed, verifying the code.

The code was then used to repeat the simulation of Kreiss and Ystrom [1]. For up to $t = 4$, the calculated solution matched the published solution [1]. However, at a later time, $t = 40$, the two solutions were quite different. Due to the simple numerical method in this work, it was assumed that the grid was simply too coarse and further refinement was required. Upon four successive refinements, it was shown that the solutions did not seem to be converging to a single solution. This nonconvergent behavior was further demonstrated using a single grid ($N = 512$) and imposing four small perturbations to the initial condition. Each slightly perturbed solution diverged from the unperturbed solution similarly to the behavior of the MMS divergence but at a significantly reduced exponential rate.

This extreme sensitivity to initial conditions indicated that the KY equations may be chaotic. Therefore, the LLE was calculated in the long-term time domain when the solution reached a quasi-steady state around the equilibrium condition. It was determined that the LLE was positive, indicating chaotic behavior, with a value of approximately 0.38. This value was

shown to quantify the rate of divergence of the perturbed initial conditions observed previously. The strange attractor was further quantified by calculating the correlation dimension. The correlation dimension was determined to be fractal with a value of 2.8. The minimum embedded dimension necessary to unfold the dynamics of the chaos was shown to be six.

The route from steady behavior to chaotic behavior was studied using the C coefficient as the control variable. For small, positive values of C, the solution approached the equilibrium steady-state solution asymptotically. As C approached a critical value C^*, the rate of decay to the equilibrium slowed until a limit cycle behavior appeared with a wavelength equal to the size of the domain, i.e., L-periodic. Further increases in C increased the amplitude of the limit cycle and the asymmetry of the waveform. Eventually, intermittency appeared: stable $L/2$-periodic waves punctuated by short bursts of chaos-like behavior. The frequency of the intermittency decreased until a stable $L/2$-periodic limit cycle was reached. A similar pattern repeated until chaotic behavior is finally reached around $C = 0.125$.

Finally, the issue of nonconvergence was re-examined. A different means to quantify the effect of the grid was sought that did not rely on comparing specific solutions at a single time. The wavenumber (Fourier) spectra of the two solution variables were averaged from times $t = 4$–40. While the different grids produce different solutions at the later time, the averaged wavenumber spectra over the time range converge to an invariant spectrum, i.e., independent of the initial conditions. This approach allows for an assessment of the numerical scheme for a particular solution depending on the desired resolution.

While some of this work may seem straightforward for the simple KY equations, it is hoped that this analysis will serve as a road map for similar analysis of the dynamic 1-D two-fluid model. It was shown that both models are similar in structure (of the PDEs), have similar linear stability properties and even have similar dynamics (waveforms). Portions of this analysis have already been used by the authors in the study of wavy-stratified liquid–liquid flow using the 1-D two-fluid model [29].

Acknowledgments

The authors would like to acknowledge funding received from Purdue University's Global Engineering Program that helped make this collaboration possible.

References

[1] H.-O. Kreiss, J. Yström, Parabolic problems which are ill-posed in the zero dissipation limit, Math. Comput. Model. 35 (2002) 1271–1295.
[2] M. Ishii, T. Hibiki, Thermo-Fluid Dynamics of Two-Phase Flow, second ed., Springer, New York, 2011.
[3] M.A. Lopez de Bertodano, W.D. Fullmer, A. Vaidheeswaran, One-dimensional two equation two-fluid model stability, Multiphase Sci. Tech. 25 (2013) 133–167.
[4] W.D. Fullmer, V.H. Ransom, M.A. Lopez de Bertodano, Linear and nonlinear analysis of an unstable, but well-posed, one-dimensional two-fluid model for two-phase flow based on the inviscid Kelvin–Helmholtz instability, Nucl. Eng. Des. 268 (2014) 173–184.
[5] G.B. Whitham, Linear and Nonlinear Waves, John Wiley & Sons, New York, 1974.
[6] H. Holmås et al, Analysis of a 1D incompressible two-fluid model including artificial diffusion, IMA J. Appl. Math. 73 (2008) 651–667.
[7] W.D. Fullmer, M.A. Lopez de Bertodano, X. Zhang, Verification of a higher-order finite difference scheme for the one-dimensional two-fluid model, J. Comput. Multiphase Flows 5 (2013) 139–155.
[8] N.P. Waterson, H. Deconinck, Design principles for bounded higher-order convection schemes – a unified approach, J. Comput. Phys. 224 (2007) 182–207.
[9] P.L. Roe, Characteristic-based schemes for the Euler equations, Ann. Rev. Fluid Mech. 18 (1986) 337–365.
[10] B. van Leer, Towards the ultimate conservative difference scheme. V. A second-order sequel to Godunov's method, J. Comput. Phys. 32 (1979) 101–136.
[11] P.H. Gaskell, A.K.C. Lau, Curvature-compensated convective transport: SMART, a new boundedness-preserving transport algorithm, Int. J. Numer. Methods Fluids 8 (1988) 617–641.
[12] D. Drikakis, W. Rider, High Resolution Methods for Incompressible and Low-Speed Flows, Springer-Verlag, Berlin, 2005.
[13] S. Gottlieb, C.-W. Shu, Total variation diminishing Runge–Kutta schemes, Math. Comput. 67 (1998) 73–85.
[14] C.-W. Shu, A survey of strong stability preserving high order time discretizations, in: D. Estep, S. Tavener (Eds.), Collected Lectures on the Preservation of Stability under Discretization, 2002, pp. 51–65.
[15] P.J. Roache, Verification and Validation in Computational Science and Engineering, Hermosa Publishers, Albuquerque, USA, 1998.
[16] P.J. Roache, Code verification by the method of manufactured solutions, J. Fluids Eng. 124 (2002) 4–10.
[17] W.L. Oberkampf, C.J. Roy, Verification and Validation in Scientific Computing, Cambridge Univ. Press, Cambridge, UK, 2010.
[18] W.L. Oberkampf, T.G. Trucano, C. Hirsch, Verification, validation and predictive capability in computational engineering and physics, Appl. Mech. Rev. 57 (5) (2004) 345–384.
[19] C.O.E. Burg, V.K. Murali, The residual formulation of the method of manufactured solutions for computationally efficient solution verification, Int. J. Comput. Fluid Dyn. 20 (7) (2006) 521–532.
[20] P.J. Roache, Perspective: a method for uniform reporting of grid refinement studies, J. Fluids Eng. 116 (1994) 405–413.
[21] J.C. Sprott, Chaos and Time Series Analysis, Oxford University Press, Oxford, UK, 2003.
[22] R.L. Machete, Quantifying chaos: a tale of two maps, Phys. Lett. A 375 (2011) 2992–2998.
[23] J.C. Sprott, Numerical calculation of the largest Lyapunov exponent, <http://sprott.physics.wisc.edu/chaos/lyapexp.htm>, 2014 (last accessed 07.01.2014).
[24] P. Grassberger, I. Procaccia, Characterization of strange attractors, Phys. Rev. Lett. 50 (5) (1983) 346–349.
[25] D. Ruelle, Chaotic Evolution and Strange Attractors, Cambridge Univ. Press, Cambridge, UK, 1989.
[26] P. Manneville, Instabilities, Chaos and Turbulence, ICP Fluid Mech., Imperial College Press, London, UK, 2010.
[27] H.D.I. Abarbanel, Analysis of Observed Chaotic Data, Springer, New York, 1996.
[28] J.M. Hyman, B. Nicolaenko, The Kuramoto–Sivashinsky equation: a bridge between PDE'S and dynamical systems, Physica D 18 (1986) 113–126.
[29] W.D. Fullmer, A. Clausse, A. Vaidheeswaran, M.A. Lopez de Bertodano, Numerical solution of wavy-stratified fluid-fluid flow with the one-dimensional two-fluid model: Stability, boundedness, convergence and chaos, in: Proc. ASME 2014 4th Joint US-Euro. Fluids Eng. Div. Summer Meet. (FEDSM), Aug. 3–7, Chicago, IL, USA, 2014.